Avalanche Photodiodes With Composite Charge-Layers for Low Dark Current, High-Speed, and High-Power Performance

Naseem, Zohauddin Ahmad, Yan-Min Liao, Po-Shun Wang, Sean Yang, Sheng-Yun Wang, Hsiang-Szu Chang, H.-S. Chen, Jack Jia-Sheng Huang, Emin Chou, Yu-Heng Jan, and Jin-Wei Shi, *Senior Member, IEEE*

***Abstract*—In this work, a novel $In_{0.52}Al_{0.48}As$ based top-illuminated avalanche photodiode (APD) is demonstrated. By combining the composite charge-layer design with a special p-side up etched mesa structure to zero the electric (E)-field at the periphery of this APD's multiplication (M-) layer, the edge breakdown phenomenon can be eliminated. This in turn leads to the simultaneous high-speed, high-saturation-power, high responsivity, and low-dark current performance characteristics of our APDs, which are essential for high-performance coherent receiver applications. The demonstrated device, with its simple top-illuminated structure exhibits a wide optical-to-electrical (O-E) bandwidth (21 GHz), high responsivity (5.5 A/W at 0.9 V_{br}), and saturation current as high as 8 mA with a large active diameter of 24 μm for easy optical alignment. Furthermore, the nonlinear driving of a wavelength sweeping laser in the self-heterodyne beating setup can generate an optical pulse train like waveform, providing an effective optical modulation depth of up to 158%, which leads to a maximum photo-generated RF power (at 10 GHz) from our APD as high as +5.5 dBm. The excellent performance of our demonstrated APDs opens up new possibilities for the next generation of coherent receivers.**

***Index Terms*—Avalanche photodiode, p-i-n photodiode.**

I. Introduction

THE OPTICAL interconnect market has boomed over the past few years. The rise in intra and inter data center traffic has led to increased bit rates and baud rates in optical communication. To accommodate this increase, a 400 Gb/s Ethernet standard has been demonstrated and is expected to be commercially available in the near future. Nevertheless, even higher data rates up to 800 Gb/s-1.6 Tb/s can be envisaged in the next generation [1]. One possible solution to attain such high data rates would be to utilize a direct-detection (DD) system with a four-level pulse amplitude modulation (PAM4) scheme. This would double the bit rates for a given baud rate. However, this type of scheme can only be effective up to a transmission distance of a few kilometers [2].

Alternatively, the integration of coherent detection with various digital processing (DSP) techniques in the telecommunication window (1.31 to 1.55 μm) could play a vital role in increasing the data rate for short and long-haul transport [3]. Due to limits in the transmitted power from the laser source, receiver sensitivity will be the key to covering the link budget for such high a bit rate at an extended communication distance. In addition, the use of heterodyne or self-heterodyne schemes for coherent detection at the receiver-end can provide a higher sensitivity than that of a DD system [4].

Compared with the DD system, for which high-speed and high-sensitivity avalanche photodiodes (APDs) or p-i-n PDs [5] are requisite, high linearity p-i-n photodiodes (PD) for wider optical-to-electrical (O-E) bandwidths, higher sensitivity, and higher saturation power are usually preferred in coherent detection systems [6]–[8]. This is because, in a coherent receiver, a weak received light can be amplified by the strong optical LO power pumping on the high-speed/-linearity PD [9]. A semiconductor optical amplifier (SOA), which is monolithically integrated with the high-power waveguide type uni-traveling carrier photodiodes (UTC-PDs) has been successfully demonstrated [10] to further enhance the optical LO power and signal-to-noise (S/N) ratio in a coherent communication system. However, for high sensitivity, this kind of integration comes at the cost of extra dc power consumption (~0.3 W) for SOA biasing (200 mA and 1.5 V) and it also increases the size of the receiver module [10], [11]. In addition, the waveguide type UTC-PDs, integrated with a well-designed spot size converter, usually exhibit a much smaller optical alignment tolerance than do their vertically illuminated counterparts integrated with a collimating lens (~5 vs. ~25 μm), [12], [13]. Replacing the high-speed waveguide

Manuscript received May 18, 2021; revised July 14, 2021 and August 10, 2021; accepted September 8, 2021. Date of publication September 13, 2021; date of current version September 29, 2021. This work was supported by the Ministry of Science and Technology in Taiwan under Grants 108-2622-E-008-011-CC2, 107-2622-E-008-002-CC2, 106-2221-E-008-063-MY3, and 109-2221-E-008 - 081 -MY3. *(Corresponding author: Jin-Wei Shi.)*

Naseem, Zohauddin Ahmad, Yan-Min Liao, Po-Shun Wang, and Jin-Wei Shi are with the Department of Electrical Engineering, National Central University, Taoyuan 320, Taiwan (e-mail: zohauddin145991@st.jmi.ac.in; karta19869871516@gmail.com; aaaa558513@gmail.com; jwshi@ee.ncu.edu.tw).

Sean Yang, Sheng-Yun Wang, Hsiang-Szu Chang, H.-S. Chen, and Emin Chou are with the Source Photonics, Science-Based Industrial Park, Hsinchu 300, Taiwan (e-mail: sean.yang@sourcephotonics.com; shengyun.wang@sourcephotonics.com; hsiangszu.chang@sourcephotonics.com; hs.chen@sourcephotonics.com; emin.chou@sourcephotonics.com).

Jack Jia-Sheng Huang and Yu-Heng Jan are with the Source Photonics, Science-Based Industrial Park, Hsinchu, Taiwan, and also with the Source Photonics, West Hills, CA 91304 USA (e-mail: jack.huang@sourcephotonics.com; yuheng.jan@sourcephotonics.com).

Color versions of one or more figures in this article are available at https://doi.org/10.1109/JSTQE.2021.3111895.

Digital Object Identifier 10.1109/JSTQE.2021.3111895

1077-260X © 2021 IEEE. Personal use is permitted, but republication/redistribution requires IEEE permission.
See https://www.ieee.org/publications/rights/index.html for more information.

Authorized licensed use limited to: National Central University. Downloaded on May 19,2022 at 05:53:44 UTC from IEEE Xplore. Restrictions apply.

p-i-n or UTC-PD with a vertically-illuminated APD structure, which has internal gain, is one of the most effective ways to increase the alignment tolerance as discussed, and improve the sensitivity performance, with less optical LO power required. The self-heterodyne beating scheme thus becomes feasible at the receiver-end, where the additional LO laser light source can be eliminated [14]. However, the saturation current of the APD is usually much smaller than that of the p-i-n or UTC-PDs. This is because the additional multiplication gain provided by the APD is sensitive to the net electric (E-) field across the active layer. The higher optical pumping power leads to a lower net E-field and less gain, which limits the maximum output current from the APD [15]. This characteristic impedes its application in coherent receivers. In this work, we demonstrate a novel p-side-up type $In_{0.52}Al_{0.48}As$ based vertically-illuminated APD with high-speed, high saturation power, and high responsivity performance. Compared to our previously reported work on APDs [16], we conduct a more detailed investigation of the static and dynamic performance of our novel APDs, which includes their gain-bandwidth product and the heterodyne-beating saturation power of APDs with different active diameters. In addition, the mechanism for enhancement of the photo-generated RF power is analyzed in detail. It can be attributed to the optical pulse train like waveform from our self-heterodyne beating light source as verified by the time-domain measurements. By incorporating a composite charge layer with a special etched-mesa structure, the E-field at the periphery of the APD's multiplication layer can be zero and the edge breakdown phenomenon can be minimized with a reduced dark current. Furthermore, a InP-based collector (transport) layer is buried below the thin M-layer of the demonstrated device. This greatly relaxes the trade-off between the RC-delay and internal transit time limited bandwidths, which can enlarge the active mesa size for the desired O-E bandwidth and enhance both the optical alignment tolerance and device heat sinking. Such a device, with a 24 μm diameter topmost active mesa, exhibits high-speed performance (21 GHz), high responsivity (5.5 A/W), and a saturation output RF power as high as +5.5 dBm (10 GHz operation frequency and 8 mA output photocurrent) under $0.9V_{br}$ operation in the self-heterodyne beating test bed. The excellent performance of our demonstrated APDs opens up new possibilities for the development of the next generation of coherent receivers.

II. Device Structure Design and Fabrication

Figs. 1 to 2 show conceptual cross-sectional views of the demonstrated device structures A and B, respectively, and their simulated E-fields in the vertical and horizontal directions. Here, two kinds of mesa structure (A and B) are fabricated to study the influence of edge breakdown on device performance. Device A is the proposed device structure to suppress the edge breakdown, which will be discussed in detail later while device B has the traditional APD structure [5]. It has a relatively weak E-field confinement because of the use of the topmost small p-type mesa. Both devices share the same

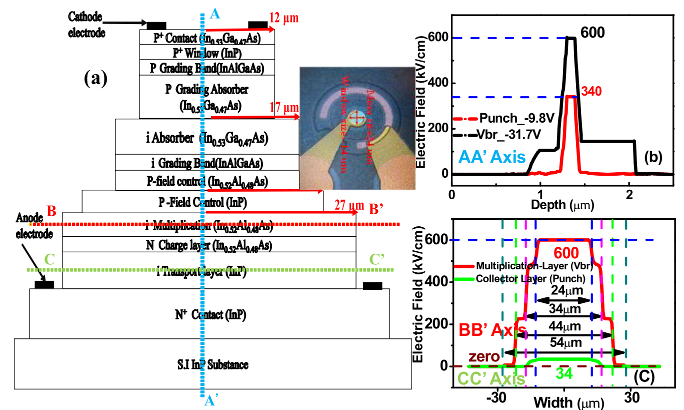

Fig. 1. (a) Conceptual cross-sectional view of Device A. Simulated E-field distributions in (b) vertical (AA') and (c) horizontal (BB') and (CC') directions. Inset shows a top-view of the fabricated device.

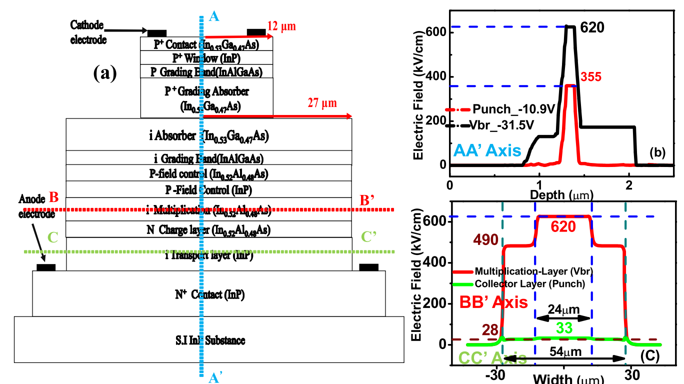

Fig. 2. (a) Conceptual cross-sectional view of Device B. Simulated E-field distributions in (b) vertical (AA') and (c) horizontal (BB') and (CC') directions.

epi-layer structure which was grown in a molecular-beam epitaxy (MBE) chamber.[1] Note that the structures are not drawn to scale for clarity of illustration. From top to bottom, the structure is composed of a p^+-$In_{0.53}Ga_{0.47}As$ contact layer, p^+-InP window layer, p-type partially depleted $In_{0.53}Ga_{0.47}As$ absorber layer, the composite p-type $In_{0.52}Al_{0.48}As$/InP charge layers, one intrinsic $In_{0.52}Al_{0.48}As$ multiplication (M-) layer, n-type $In_{0.52}Al_{0.48}As$ charge layer, a thick ($\sim$0.6 μm) InP collector (transport) layer, and the bottommost InP n^+ contact layer. Details of the material composition, thickness, and doping density of each layer are given in Table I. The partially depleted p-type absorber has a graded doping profile in the p-type layer (top: 5×10^{18} to bottom: 5×10^{16}cm^{-3}) to shorten the hole transit time, accelerate the electron diffusion process, and increase the high-power and linearity performance of our APD [17]. There are two major differences in the epi-layer structures between our devices and other previously reported high-speed APDs [5], [17], [18]. Firstly, our charge layer is composed of hetero-junctions ($In_{0.52}Al_{0.48}As$/InP). Selective wet etching is

[1]Intelligent Epitaxy Technology, Inc., 1250 E Collins Blvd, Richardson, TX 75081.

Authorized licensed use limited to: National Central University. Downloaded on May 19,2022 at 05:53:44 UTC from IEEE Xplore. Restrictions apply.

TABLE I
EPITAXIAL STRUCTURES

	APD-PD			
	Material	Thickness (Å)	Doping Level (/cm³)	Type
P-Contact layer	$In_{0.53}Ga_{0.47}As$	1000	1.0E+19	p+
Window	InP	5000	5.0E+18	p+
P-Grading band	$In_{0.53}Ga_{0.47}As$ /$In_{0.52}Al_{0.48}As$	120	5.0E+18	p+
P-Absorption layer	$In_{0.53}Ga_{0.47}As$	3700	5E+18 (top) to 5E+16 (bottom)	p
i-Absorption layer	$In_{0.53}Ga_{0.47}As$	2000	<2E+15	
i-Graded band	$In_{0.53}Ga_{0.47}As$ /$In_{0.52}Al_{0.48}As$	40		
P-field control	$In_{0.52}Al_{0.48}As$	600	3.5E+17	P
P-field control	InP	300	6.5E+17	P
i-Multiplication	$In_{0.52}Al_{0.48}As$	880		
N-Charge layer	$In_{0.52}Al_{0.48}As$	750	4E+17	N
i-Transport layer	InP	6000		
N-Contact layer	InP	10000	>1.0E+19	N+
S.I-InP Substrate	InP			

performed to etch away the charge layer above the M-layer and zero the electric-field at the mesa side-wall. Second, we insert a thicker InP transport layer, which can effectively relax the burden imposed on the RC-limited bandwidth and enlarge the active diameter, further improving the output saturation power. Compared to the inverted p-side down APD structure [17], our demonstrated n-side-down structure may benefit the high-power performance due to that in our structure the high E-field region (at the M-layer) is buried at the bottom, close to the InP substrate, which allows for good device heat sinking. Fig. 1(a) shows the quintuple mesa structure adopted to confine the E-field in the first mesa (active region) with a diameter of 24 µm, which is etched through the p-type window layer and the p-type absorber layer, stopping at the un-doped absorption layer. The second mesa underneath the first mesa has a diameter of 34 μm, which includes the first $In_{0.52}Al_{0.48}As$ charge layer. Selective etching stops at the second InP charge layer. The capping InP charge layer above the M-layer is etched to form the third mesa (44 μm in diameter). The strong E-field at the periphery of the bottom M-layer can be zero and confined within the range of the first mesa (24 μm diameter). The electric field distribution within the device is simulated by using the Silvaco Technology Computer Aided Design (TCAD) tools.[2] Figs. 1 and 2 show the electric fields calculated for devices A and B, respectively, along the vertical direction (AA') at the punch-through (V_{pt}), breakdown voltage (V_{br}) and in the horizontal direction (BB') in the M-layer at V_{br} and in the (CC') direction in the transport layer at V_{pt}.

As can be seen in Figs. 1(b) and 2(b), by properly adjusting the doping density in the charge layers, the simulated E-fields in the InP transport (170 kV/cm) and in the depleted $In_{0.53}Ga_{0.47}As$ absorption layer (130 kV/cm) at the AA' axis under a V_{br} (-31.5 V) bias are less than their critical fields (150 kV/cm for $In_{0.53}Ga_{0.47}As$ and 500 kV/cm for InP) [19]. Furthermore, in contrast to device B, which has high E-fields in the side walls

[2]Silvaco, 2811 Mission College Boulevard, 6th floor, Santa Clara, CA 95054.

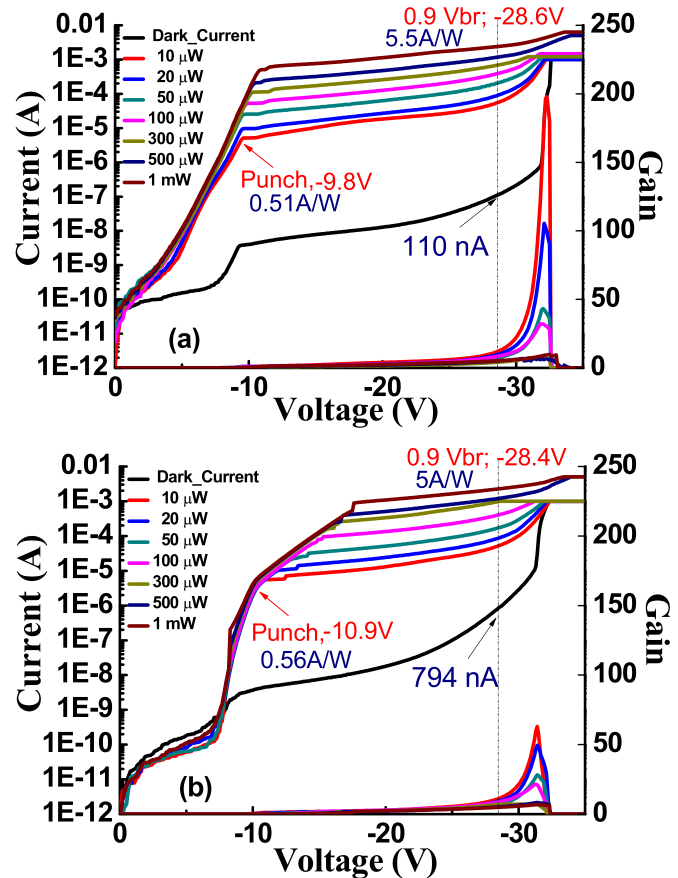

Fig. 3. The measured dark current, photocurrent, and operation gain versus bias voltage under different optical pumping powers at 1.31 μm wavelength for 20 μm active window sized APDs (a) Device A and (b) Device B.

of the M-layer (~500 kV/cm at V_{br}) and the transport layer (28 kV/cm at V_{pt}), the E-field in these regions in device A can be exactly zero. This is due to the removal of the charge layer above it by InP/InAlAs selective wet etching in our novel composite charge layer design with the special mesa structure, as discussed above. The insert to Fig. 1(a) shows a top view of the fabricated device A with a 24 μm mesa active diameter. The corresponding optical window diameter is 14 μm.

III. Device Measurement Results

Figs. 3(a) and (b) show the measured bias-dependent dark current, photocurrent, and operation gain of the demonstrated devices A and B, respectively, subject to different optical pumping powers at the optical wavelength of 1.31 μm. Both devices have the same 20 μm diameter topmost active window size. The breakdown voltage (V_{br}) is around 31 V and the corresponding dark current at 0.9 V_{br} is around 100 nA for device A. As can be seen, device A exhibits a much lower dark current than does device B due to the elimination of edge breakdown, as illustrated in Fig. 1. A further lowering of the dark current of device A can be realized by increasing the charge layer doping density to reduce the E-field in the absorber at the expense of a narrower operating

Authorized licensed use limited to: National Central University. Downloaded on May 19,2022 at 05:53:44 UTC from IEEE Xplore. Restrictions apply.

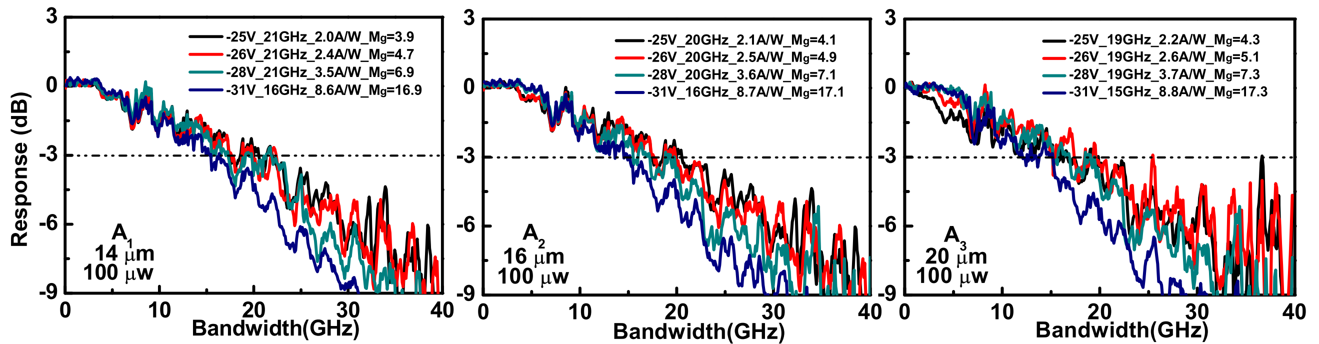

Fig. 4. The measured bias dependent O-E frequency responses of Devices A_1 to A_3 under a low 100 μW optical pumping power at the 1.31 μm wavelength.

window between V_{pt} and V_{br}. Compared with device B, device A exhibits less of an increase in V_{pt} with the increase in input power, which can be attributed to stronger E-field confinement and less current spreading in the lateral direction in the transport layer, as shown in Fig. 1(c) and 2(c). Under 0.9 V_{br} and with a low value of launched optical power ($\sim$10 μW), the measured responsivity is around 5.5 A/W. We adopted a lens fiber having a spot size of around 2 μm, which is much smaller than the diameter of our active window to ensure nearly zero optical coupling loss and a single pass of injected light into the absorption layer. The theoretical maximum unit gain responsivity for the device fabricated with a 0.57 μm-thick $In_{0.53}Ga_{0.47}As$ absorption layer will be around 0.46 A/W at the 1.31 μm wavelength. The corresponding maximum external quantum efficiency is 43.5%. Here, the photo-absorption constant used for the $In_{0.53}Ga_{0.47}As$ layer at a wavelength of 1.31 μm is around 1.0 μm^{-1} [20]. Some reported work claims unity gain using punch through (V_{pt}) responsivity [17], considering that, in our device the unit gain responsivity is chosen at V_{pt} with 0.51 A/W responsivity. As can be seen, based on the value of the theoretical maximum responsivity (0.46 A/W), the multiplication gain under V_{pt} is slightly more than 1. This is because our charge layer doping density is high enough to suppress the absorption layer breakdown and let the E-field in the M-layer be around its critical field when the bias voltage just reaches V_{pt} [21]. The gain versus bias voltage under different optical pumping powers (10 to 1000 μW) is also provided in the figures for reference. As can be seen, there is a significant reduction in all the measured operation gains when the reverse bias voltage is over V_{br} due to the tremendous increase in the dark current, which occupies most of the measured total current (i.e., summation of photocurrent and dark current). In addition, we can clearly see that the maximum operation gain gradually decreases with an increase in the pumping power. This phenomenon can be explained by the space charge screening (SCS) effect induced by the photogeneration of holes in the undoped $In_{0.53}Ga_{0.47}As$ absorption layer, which reduces the net E-field and multiplication gain in the M-layer [15].

In order to accurately extract the internal carrier transit time of our demonstrated APD, which will be discussed in detail later, we fabricate device A with three different diameters (A_1 to A_3) of active mesa (window) of 24 (14), 26 (16) and 30 (20) μm respectively. Figs. 4 and 5 show the 3-dB O-E frequency responses at the 1.31 μm wavelength of the three devices A_1 to A_3, under low (0.1 mW) and high (1 mW) optical pumping powers, respectively. We can clearly see that under a bias of around 0.9 V_{br} (-28 V), all three devices can sustain a 3-dB bandwidth of approximately 20 GHz across a wide range of optical pumping powers. Such invariant high-speed performance can be attributed to the significant decrease in the value of the operation gain, making them much less sensitive to the reverse bias voltage under high-power operation, as shown in Fig. 3. We can also see some slight variation in the responsivity for these three devices, which can be attributed to the collection of some residual light at the periphery of the focal spot by the larger optical window (14 to 20 μm). The delay time induced by the avalanche gain, which is the major bandwidth limiting factor of an APD under high-bias operation is thus minimized, resulting in the observed invariance of the 3-dB O-E bandwidth [15]. Fig. 6(a) shows the 3-dB O-E bandwidths versus operation gains of device A_1 measured under low (0.1 mW) and high (1 mW) optical pumping powers. As can be seen, for the low pumping power case, our demonstrated device can achieve a gain-bandwidth (GB) product as high as 336 GHz with a 0.51 A/W unit-gain responsivity under the high-gain regime. The key reason for defining the GBP value at extremely high gain is because this number represents the limitations of maximum intrinsic speed performance of the APD [21]. In contrast, at operational conditions, the GB product is around 272 GHz. The GB product gradually decreases to 140 GHz when the optical pumping power reaches 1 mW. This can be attributed to the reduction in the multiplication gain (8.8 to 5.1) versus the increase of optical power as discussed above. The high GB product (336 GHz) can be attributed to the aggressive downscaling of the M-layer and the absorber thicknesses and the significant effect of dead space effect the M-layer [15]. Moreover, the GB curves or our devices, with their composite layer design, show different trends compared with the gain-bandwidth curves of typical APDs, which usually have single charge layers and exhibit a monotonic decrease of bandwidth with the increase of the multiplication gain. As highlighted by the red circle in Fig. 6(a), the decrease of bandwidth under very high operation gain (>20) is gradually minimized at low (0.1 mW) power excitation. This phenomenon may be attributed to the additional InP

Authorized licensed use limited to: National Central University. Downloaded on May 19,2022 at 05:53:44 UTC from IEEE Xplore. Restrictions apply.

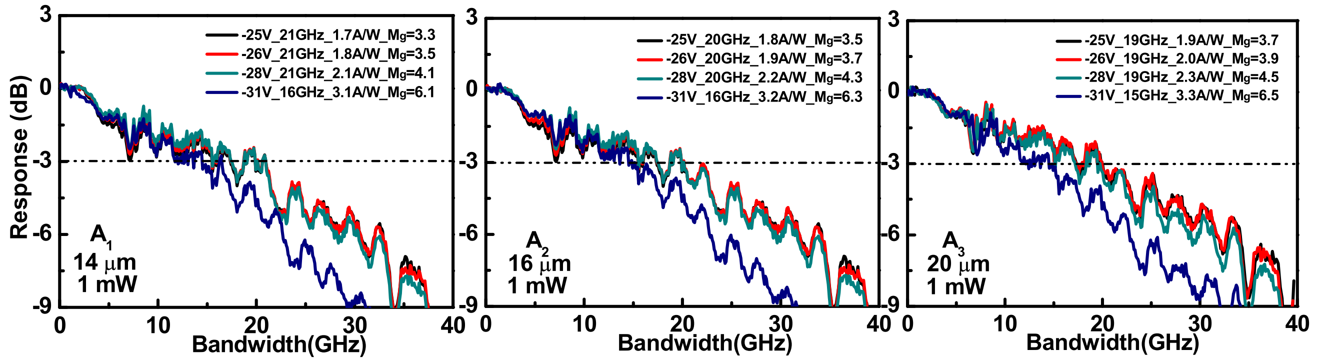

Fig. 5. The measured bias dependent O-E frequency responses of Devices A_1 to A_3 under a low 1 mW optical pumping power at the 1.31 μm wavelength.

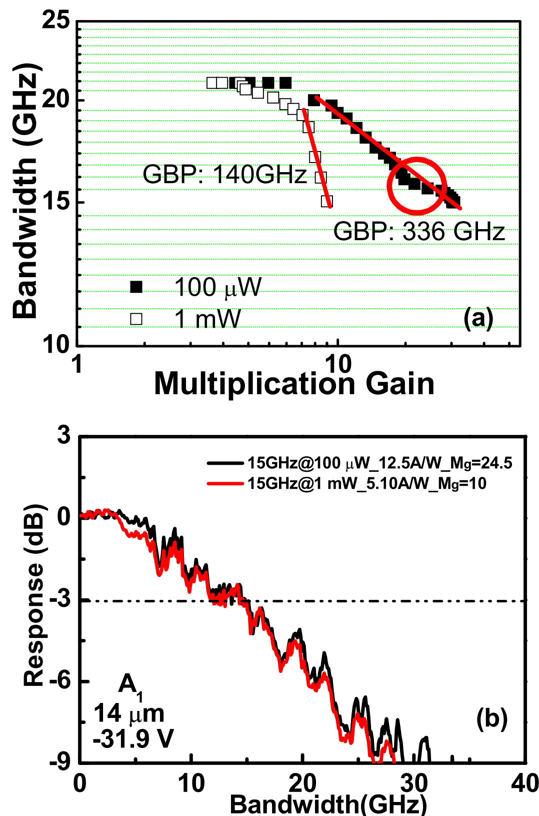

Fig. 6. (a) The measured 3-dB O-E bandwidths versus multiplication gain and (b) Measured O-E responses at low (100 μW) and high (1 mW) optical pumping powers for the demonstrated A_1 under V_{br} bias. The trend of the GB curves under high-gain operation is highlighted by the red circle, as shown in (a).

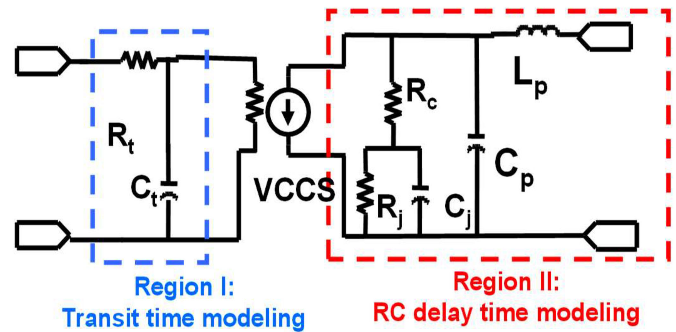

Fig. 7. Equivalent-circuit-model. VCCS: Voltage controlled current source.

charge layer just above the $In_{0.52}Al_{0.48}As$ M-layer, which also contributes the multiplication gain under high-bias (gain) operation. It can avoid the InAlAs based M-layer being pushed into the deep avalanche region for very high-gain operation, thereby releasing the bandwidth reduction under near V_{br} operation. This is similar to the behavior of APDs with dual M- and charge layers reported in our previous work [15]. The corresponding bandwidth-responsivity product is quite close to that reported for the N-side up $In_{0.52}Al_{0.48}As$ based APD (~171 vs. ~189 [17] GHz × A/W) with the same M-layer thickness (~90 nm).

Fig. 6(b) shows the corresponding O-E responses measured under low and high power operation. As we can clearly see, the measured bandwidths are pinned at around 15 GHz, regardless of the gain. thereby resulting in the high gain-bandwidth product, as discussed above.

The overall O-E 3-dB bandwidth (f_{3dB}) of the APDs is determined by the carrier transport time ($1/f_t$) and the RC time constant ($^1/_{f_{RC}}$). The bandwidth limiting factor of our demonstrated device is calculated using the following equation adopted from [15], [22]:

$$\frac{1}{f_{3dB}^2} = \frac{1}{f_{RC}^2} + \frac{1}{f_t^2} = (2\pi RC)^2 + \frac{1}{f_t^2}, \qquad (1)$$

where R is the sum of the parasitic resistance and the load resistance (50 Ω) and C is the total capacitance. Here, we perform the equivalent circuit modeling technique to extract the RC-limited bandwidths of our devices by fitting the measured scattering parameters of the microwave reflection coefficients (S_{22}) [15]. Fig. 7 shows the equivalent circuit models adopted to fit the S_{22} parameters of the devices. The fitted values of each circuit element are shown Table II. The Smith charts in Figs. 8(a) to (c) show the fitted and measured frequency responses corresponding to the S_{22} parameters for devices A_1 to A_3. Clearly, there is a good match between the simulated and measured results. During the modeling process for the extraction of the extrinsic f_{RC} of the APD chips, the two artificial circuit elements, R_T and C_T, are removed.

Authorized licensed use limited to: National Central University. Downloaded on May 19,2022 at 05:53:44 UTC from IEEE Xplore. Restrictions apply.

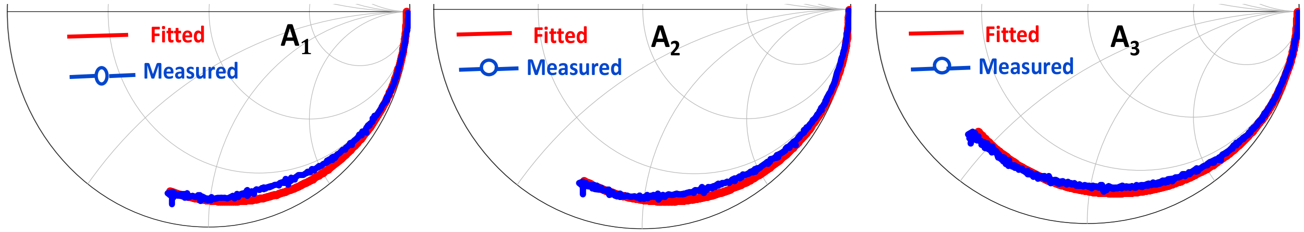

Fig. 8. The measured (blue line) and fitted (red line) S_{22} parameters from near dc to 40 GHz under a fixed dc bias (-28 V) for demonstrated devices A_1 to A_3.

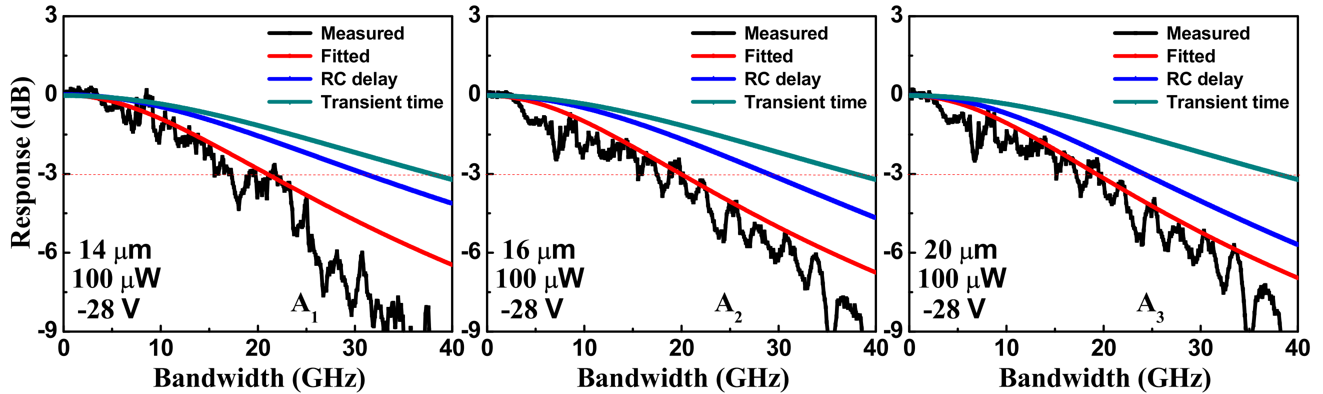

Fig. 9. The measured O-E, extracted RC-limited, transit time, and fitted O-E frequency responses for demonstrated devices A_1 to A_3.

TABLE II
VALUES OF THE CIRCUIT ELEMENTS

	Physical Meaning	Devices		
		A_1	A_2	A_3
Cj	Junction Capacitance (fF)	53	60	86
Rc	Junction Resistance (kΩ)	12	12	12
Rs	Contact Resistance (Ω)	21	21	21
Cp	Parasitic Capacitance (fF)	45	45	56
Lp	Parasitic Inductance (pH)	8.5	16.1	31.1

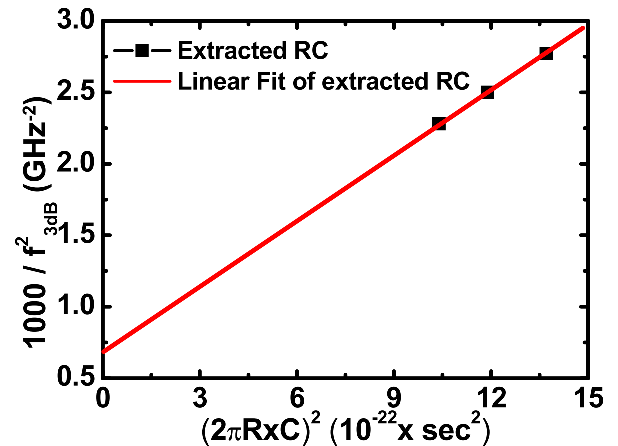

Fig. 10. The extracted $(1/f_{RC})^2$ versus the measured $(10^3/f_{3dB}^2)$ for devices A_1 to A_3.

This is because they are used to mimic the low-pass frequency response of the internal carrier transit time [23], [24]. By choosing the proper values of R_T and C_T to fit the measured O-E frequency response, we can then determine the internal transit time limited frequency responses of our devices. Figs. 9(a) to (c) show the measured O-E, fitted O-E, extracted RC-limited and transit time limited frequency responses under −28 V for devices A_1 to A_3, respectively. As can be seen, the RC-limited bandwidths for devices A_1 and A_2 are close to the transit time limited ones, around 38 GHz. This indicates that the total depletion layer thickness is nearly optimal to balance the internal carrier transit time and external RC-limited bandwidth for the 24 and 26 μm active mesa diameter devices. Another way to extract the internal carrier transit time is based on Equation 1 as discussed above. Fig. 10 shows the $(1/f_{RC})^2$ versus $(10^3/f_{3dB}^2)$ values for the demonstrated APDs (A_1 to A_3). Through the use of Equation 1 and the fitted RC- limited and measured net O-E bandwidths for each device, as illustrated in Figs. 8 and 9, the internal carrier transit time in our device can be determined from the intercepts along the y-axis in this figure [15], [22]. The obtained f_t is around 38 GHz, which is consistent with the transit time limited bandwidth (around 38 GHz) obtained by the equivalent circuit modeling technique, as shown in Fig. 9.

In contrast to the p-i-n PD based heterodyne receiver for coherent transmission, the LO laser source may be eliminated

Authorized licensed use limited to: National Central University. Downloaded on May 19,2022 at 05:53:44 UTC from IEEE Xplore. Restrictions apply.

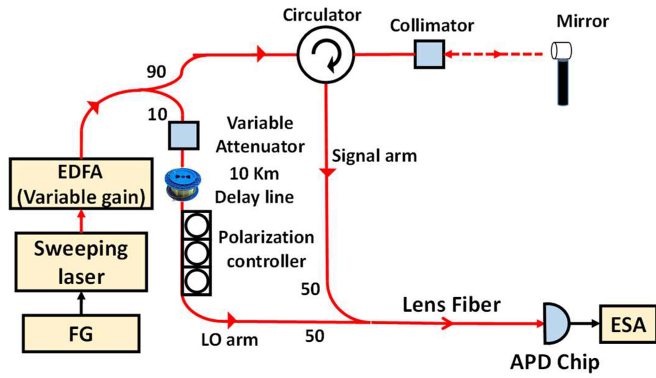

Fig. 11. Conceptual diagram of our self-heterodyne beating system. FG: function generator.

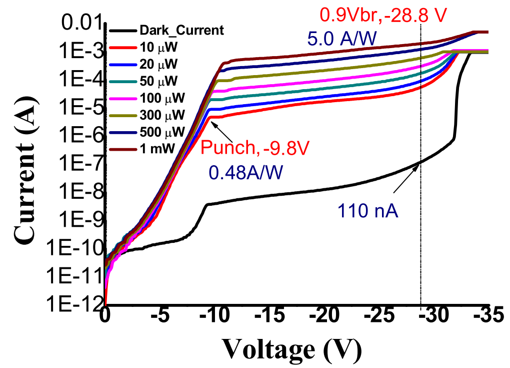

Fig. 12. The measured dark current and photocurrent versus bias voltage under different optical pumping powers at 1.55 μm wavelength for 20 μm active window sized APDs.

in the APD-based receiver. This self-heterodyne (homodyne) beating approach becomes feasible due to the large internal gain [14] which can greatly reduce the required power consumption and further improve the sensitivity performance. Here, we establish a self-heterodyne beating setup to study the high-power performance of our APD. As illustrated in Fig. 11, this system is driven by a wavelength sweeping laser (for more detail about this sweeping laser the interested reader can refer to our previous work [25]), which can generate linear/nonlinear chirped optical waveforms by AC signal modulation. The laser source is split into the signal path and the LO path using a 90/10 fiber splitter. A larger ratio of optical power is allocated to the signal arm (90 to 10) because of the significant free space diffraction and collection loss. The signal light passes through the circulator and fiber collimator to produce a beam in free space which illuminates a metal plate acting as a mirror. The weak reflected light in free space, usually with a power of tens of μW, is collected by the collimator and then redirected by the circulator to follow a different path. Finally, the signal is combined with the optical LO power via a 50/50 fiber splitter, to produce a stable self-heterodyne beating signal. A variable attenuator is included in the LO path to balance the optical power between the signal and the LO arm and maximize the photo-generated RF power. By tuning the optical delay line length, which is a 10 km fiber cable spool, and the driving condition of our sweeping laser, we can generate a beating signal with a frequency of 10 GHz. A longer delay line leads to a higher self-heterodyne beating frequency, however, due to the limitation in the coherency of our sweeping laser, the maximum self-heterodyne beating frequency in our setup is limited to 10 GHz. This 10 GHz beating signal is then fed to our demonstrated APD chip for coherent detection. The output photocurrent of the APD can be controlled by tuning the gain of the Erbium-Doped Fiber Amplifier (EDFA). Fig. 12 shows the measured bias-dependent dark current and photocurrent of the demonstrated device A_3 subjected to different optical pumping powers at the optical wavelength of 1.55 μm. We can clearly see that our device exhibits almost the same responsivity ($\sim$5 A/W @ 0.9 V_{br}) at both the 1.31 and 1.55 μm wavelengths. Thus, the influence of the wavelength shift has less significance (1.31 to 1.55 μm) for system performance. We can thus expect that for lidar application, where eye safety is a critical issue, a setup based on the demonstrated APD (1.55 μm wavelength) is a better choice than one operating at 1.31 μm. Fig. 13 shows the measured photo-generated RF power at 10 GHz versus output photocurrent of devices A_1 to A_3 at different reverse bias voltages in the self-heterodyne beating setup, as described above. The pink trace represents the ideal line (100% optical modulation depth) of photo-generated RF power from a PD with an infinite bandwidth and integrated with a 50 Ω load.

As can be seen in Fig. 13, the output power from all three devices is around 3-4 dB larger than that of the ideal line under the same output photocurrent at 0.9 V_{br}. The corresponding optical modulation depth in our self-heterodyne beating system is about 158%. This can be attributed to the fact that the optical waveform generated from our sweeping laser is close to the optical pulse train, with a 10 GHz repetition rate, instead of being a perfect 10 GHz sinusoidal signal [9]; this will be discussed in greater detail later. The maximum 10 GHz output power of the three devices is almost the same and can be as high as +5.5 dBm (for device A_3) under a bias of around 0.9 V_{br} and 8 mA output photocurrent. Under such a high output power, the measured responsivity is around $\sim$3 A/W. This output RF power value appears to be the highest recorded for all reported high-speed APDs [14], [17]. Overall, the simultaneously large maximum RF output power (5.5 dBm) and high-responsivity ($\sim$3 A/W) demonstrated by our APD demonstrates its potential to replace the high-speed p-i-n PDs in coherent receivers.

Fig. 13 shows the photo-generated RF output power obtained by using the heterodyne (20 GHz) beating set-up under different V_{br} for these three devices. Here, the heterodyne-beating system is composed of two free-running lasers operating around the 1.55 μm optical wavelength with a 20 GHz (0.16 nm) spacing in their central wavelengths. We can clearly see that of these three devices (A_1 to A_3), device with the smallest active diameter (14 μm; A_1) shows lowest saturation current ($\sim$7 vs. 8 vs. 9 mA), under 0.9 V_{br} bias. On the other hand, all three devices exhibit the same values of saturation current (power) under the self-heterodyne beating scheme. This can be attributed to the waveform of the launched signal being optical pulse like with a 30% duty cycle, as discussed below. Such a low duty cycle

Authorized licensed use limited to: National Central University. Downloaded on May 19,2022 at 05:53:44 UTC from IEEE Xplore. Restrictions apply.

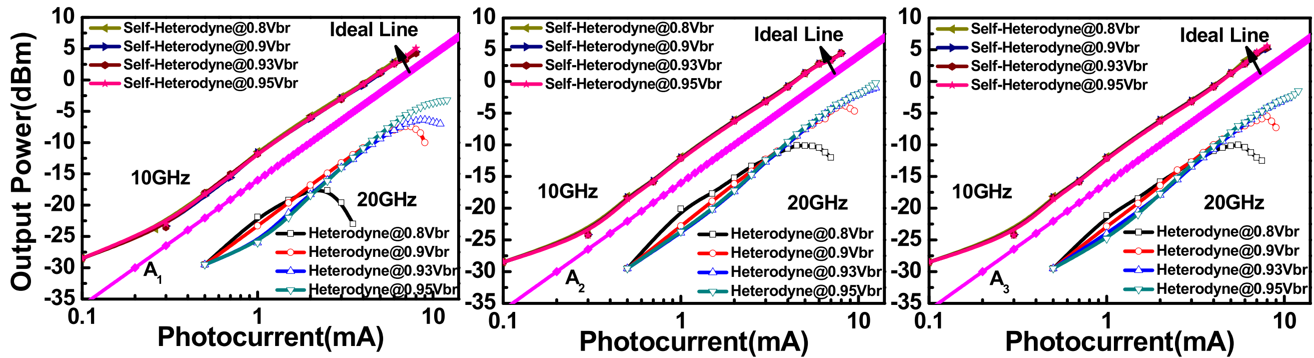

Fig. 13. The measured photo generated RF power versus photocurrent for devices A_1 to A_3 at frequencies 10 and 20 GHz for self-heterodyne and heterodyne beating under different bias voltages, respectively.

optical pulse train can minimize the device heating/saturation phenomenon, leading to the close maximum RF power (current) values. The maximum power is limited by device failure under high power operation. For self-heterodyne beating, there is a significant improvement in the RF output power, as much as 9 dB, under the same output photocurrent (8mA), compared to that obtainable with the heterodyne-beating setup. The measured O-E responses in Fig. 9 clearly show a 3-dB high-frequency roll-off at an operating frequency of 20 GHz. By de-embedding this 3-dB roll-off in the traces of heterodyne-beating power at 20 GHz, as shown in Fig. 13, there is still a 6 dB enhancement of the self-heterodyne beating RF power exhibited under the same output photocurrent. This corresponds to a tremendous increase (70% vs. 158%) in the optical modulation depth. This advantage will in turn lead to less optical LO power being required, thereby effectively increasing the power budget in the self-heterodyne beating coherent receiver system. Such an enhancement can be attributed to the distortion of the generated sinusoidal optical waveform from our sweeping laser source under large-signal driving conditions (200 kHz, 1.7 V_{pp}), which leads to the optical pulse like waveform. Optical modulation depths of over 100% have been reported using an optical pulse shaper [26], semiconductor mode-locked laser [27], and electro-optical (E-O) modulator under class AB operation [28] for the photo-generated microwave and millimeter-wave power.

In order to precisely characterize the optical waveform generated from our self-heterodyne beating system, a fast optical receiver (PT-40D/8XLMD) connected with a real-time scope (MSO 72504DX), which can provide a less than 10 ps time resolution, is adopted to measure the generated optical waveform. Fig. 14(a) shows the captured time-domain waveforms. As can be seen, the distorted sinusoidal wave behaves like an optical pulse train with a full-width half maximum (FWHM) pulse-width of 0.03 ns and a pulse repetition rate (PRR) of 0.1 ns. The obtained pulse like waveform thus results in the observed high (>100%) optical modulation depth. Fig. 14(b) shows the measured photo-generated RF spectra output from device A_1 under different output photocurrents. The occurrence of a strong harmonic frequency at 20 GHz reflects the fact that the launched optical signal has a short-pulse waveform. This is consistent with the time-domain measurement results as illustrated in Fig. 14(a).

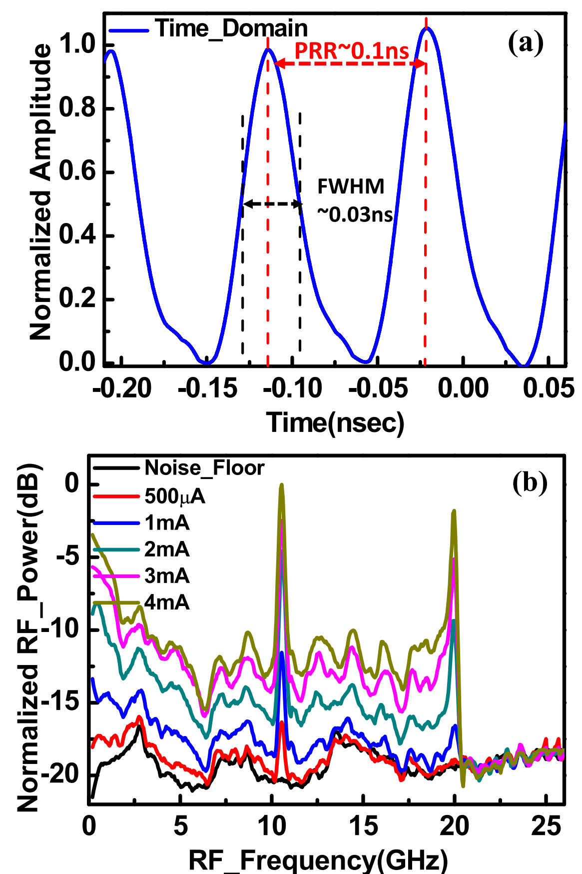

Fig. 14. (a) Captured time domain waveform generated from sweeping laser using fast optical receiver (PT-40D/8XLMD) and (b) RF spectra under different photocurrent outputs at 0.9 V_{br} of our demonstrated APDs.

IV. Conclusion

In conclusion, we demonstrate a novel top-illuminated APD structure with excellent high-speed and high-power performance. By utilizing p-side up and composite charge layers with a special mesa structure, the E-field can be strongly confined in the center of the In0.52Al0.48As based M-layer, which greatly suppresses the edge breakdown phenomenon and leads to a much lower dark current. Moreover, compared to the inverted n-side

Authorized licensed use limited to: National Central University. Downloaded on May 19,2022 at 05:53:44 UTC from IEEE Xplore. Restrictions apply.

up APD structure, which has excellent E-field confinement, our demonstrated p-side-up structure has the advantage of higher power performance due to better heat dissipation where the high E-field region (at the M-layer) is buried at the bottom, close to the InP substrate. By optimizing the depletion width of the partially p-doped $In_{0.53}Ga_{0.47}As$ absorber and additional InP collector layer to balance the RC-delay time and internal transit time. Thus, our demonstrated APDs can have a large active diameter of 24 μm for large optical alignment tolerance and good device heat sinking. Under a 0.9 V_{br} bias, this 24 μm active mesa diameter device can attain a wide O-E bandwidth (21 GHz), a high responsivity (5.5 A/W), and a saturation output RF power of over +5.5 dBm at 10 GHz when tested in a self-heterodyne beating system. The excellent dynamic/static performance demonstrated by our APD opens up new ways to further improve the sensivity performance of photoreceivers in coherent communication and frequency modulated continuous wave (FMCW) lidar systems.

REFERENCES

[1] [Online]. Available: https://ethernetalliance.org/technology/2020-roadmap/
[2] M. Nada, T. Yoshimatsu, F. Nakajima, K. Sano, and H. Matsuzaki, "A 42-GHz bandwidth avalanche photodiodes based on III-V compounds for 106-Gbit/s PAM4 applications," *J. Lightw. Technol.*, vol. 37, no. 2, pp. 260–265, Jan. 2019.
[3] C. Xie and J. Cheng, "Coherent optics for data center networks," in *Proc. IEEE Photon. Soc. Summer Topicals Meeting Ser.*, Cabo San Lucas, Mexico, Jul. 2020, pp. 1/2.
[4] J. Cheng *et al.*, "Comparison of coherent and IMDD transceivers for intra datacenter optical interconnects," in *Proc. Opt. Fiber Commun. Conf. Exhib.*, San Diego, CA, USA, Mar. 2019, Art. no. W1F.2.
[5] B. F. Levine *et al.*, "A new planar ingaas-inalas avalanche photodiode," *IEEE Photon. Tech. Lett.,* vol. 15, pp. 1898–1900, Sep. 2006.
[6] C. V. Poulton *et al.*, "Coherent solid-state LIDAR with silicon photonic optical phased arrays," *Opt. Lett.,* vol. 42, no. 20, pp. 4091–4094, Oct. 2017.
[7] P. J. M. Suni, J. E. Bowers, L. Coldren, and S. J. Ben Yoo, "Photonic integrated circuits for coherent lidar," in *Proc. 18th Coherent Laser Radar Conf.*, Boulder, CO, USA, Jun. 2016, pp. 1–6.
[8] S. Crouch, "Advantages of 3D imaging coherent lidar for autonomous driving applications," in *Proc. 19th Coherent Laser Radar Conf.,* Okinawa, Japan, Jun. 2018, pp. 1–4.
[9] P. Adany, C. Allen, and R. Hui, "Chirped lidar using simplified homodyne detection," *J. Lightw. Technol.*, vol., vol. 27, pp. 3351–3357, Aug. 2009.
[10] M. Anagnosti *et al.*, "Record gain x bandwidth (6.1 THz) monolithically integrated SOA-UTC photoreceiver for 100-Gbit/s applications," *J. Lightw. Technol.*, vol. 33, pp. 1186–1190, Mar. 2015.
[11] Y.-T. Han *et al.*, "A compact 100G-ER4 ROSA realized by hybrid integration of SOA and lensed PIN-PDs for QSFP28 transceivers," in *Proc. Opt. Fiber Commun. Conf. Exhib.*, San Diego, CA, USA, Mar. 2019, Art. no. W3E.3.
[12] J.-S. Choe *et al.*, "Optimization of spot-size converter for low polarization dependent loss of waveguide photodetector," *Opt. Exp.*, vol. 21, no. 25, pp. 30175–30182, Dec. 2013.
[13] J. Y. Huh, S.-K. Kang, J. H. Lee, J. K. Lee, and S. M. Kim, "Highly alignment tolerant and high-sensitivity 100 Gb/s (4 × 25 Gb/s) APD-ROSA with a thin-film filter-based de-multiplexer," *Opt. Exp.,* vol. 24, no. 24, pp. 27104–27114, Nov. 2016.
[14] P. Runge *et al.*, "Waveguide integrated balanced photodetectors for coherent receivers," *IEEE J. Sel. Topics Quantum Electron.,* vol. 24, no. 2, Mar./Apr. 2018, Art. no. 6100307.
[15] H.-Y. Zhao *et al.*, "High-Speed avalanche photodiodes with wide dynamic range performance," *J. Lightw. Technol.*, vol. 37, no. 23, pp. 5945–5952, Dec. 2019.
[16] Naseem *et al.*, "High-Speed and high saturation power avalanche photodiode for coherent communication," in *Proc. Opt. Fiber Commun. Conf.*, Jun. 2021, Art. no. F2C.5.
[17] M. Nada, Y. Yamada, and H. Matsuzaki, "Responsivity-Bandwidth limit of avalanche photodiodes: Toward future ethernet systems," *IEEE J. Sel. Topics Quantum Electron.*, vol. 24, no. 2, Mar./Apr. 2018, Art. no. 3800811.
[18] E. Ishimura *et al.*, "Degradation mode analysis on highly reliable guarding-free planar InAlAs avalanche photodiodes," *IEEE/OSA J. Lightw. Technol.*, vol. 25**,** pp. 3686–3693, Dec. 2007.
[19] Y. L. Goh, J. S. Ng, C. H. Tan, W. K. Ng, and J. P. R. David, "Excess noise measurement in $In_{0.53}Ga_{0.47}As$," *IEEE Photon. Technol. Lett.*, vol. 17, no. 11, pp. 2412–2414, Nov. 2005.
[20] M. S. Park and J. H. Jang, "$GaAs_{0.5}Sb_{0.5}$ lattice matched to InP for 1.55 μm photo-detection," *Electron. Lett.*, vol. 44, no. 8, pp. 549–551, Apr. 2008.
[21] G. S. Kinsey, J. C. Campbell, and A. G. Dentai, "Waveguide avalanche photodiode operating at 1.55 μm with a gain-bandwidth product of 320 GHz," *IEEE Photon. Tech. Lett.*, vol. 13, pp. 842–844, Aug. 2001.
[22] K. Kato, "Ultrawide-Band/High-Frequency photodetectors," *IEEE Trans. Microw. Theory Techn.*, vol. 47, no. 7, pp. 1265–1281, Jul. 1999.
[23] Naseem, "The enhancement in speed and responsivity of uni-traveling carrier photodiodes with $GaAs_{0.5}Sb_{0.5}/In_{0.53}Ga_{0.47}As$ type-II hybrid absorbers," *Opt. Exp.,* vol. 27, no. 11, pp. 15495–15504, May 2019.
[24] Y.-S. Wu; J.-W. Shi; P.-H. Chiu, "Analytical modeling of a high performance near-ballistic uni-traveling-carrier photodiode at a 1.55 μm wavelength," *IEEE Photon. Technol. Lett.,* vol. 18, no. 8, pp. 938–940, Apr. 2006.
[25] Z. Ahmad *et al.*, "Avalanche photodiodes with dual multiplication layers and ultra-high responsivity-bandwidth products for FMCW lidar system applications," *IEEE J. Sel. Topics Quantum Electron.*, vol. 8, no. 2, Mar./Apr. 2022, Art. no. 3800709, doi: 10.1109/JSTQE.2021.3062637.
[26] F.-M. Kuo *et al.*, "Spectral power enhancement in a 100-GHz photonic millimeter-wave generator enabled by spectral Line-by-Line pulse shaping," *IEEE Photon. J.,* vol. 2, no. 5, pp. 719–727, Oct. 2010.
[27] A. Hirata, M. Harada, and T. Nagatsuma, "120-GHz wireless link using photonic techniques for generation, modulation, and emission of millimeter-wave signals," *J. Lightw. Technol.*, vol. 21, no. 10, pp. 2145–2153, Oct. 2003.
[28] D. Tulchinsky *et al.*, "High-Current photodetectors as efficient, linear, and high-power RF output stages," *J. Lightw. Technol.*, vol. 26, no. 4, pp. 408–416, Feb. 2008.

Naseem was born in Punjab, India, in 1991. He received the M. Tech. degree from the Department of Nanotechnology, Jamia Millia Islamia, New Delhi, India. He is currently working toward the Ph.D. degree from the Department of Electrical Engineering, National Central University, Taiwan. His current research interests include high-speed photodiodes and avalanche photodiode for optical receiver.

Zohauddin Ahmad was born in Bihar, India, in 1989. He graduated from the Department of Nanoscience and Nanotechnology, Jamia Millia Islamia, New Delhi, India. He is currently working toward the Ph.D. degree from the Department of Electrical Engineering, National Central University, Taiwan. His current research interests include high-speed modulator-based lasers, FMCW-Lidar and photonics integrated circuits.

Yan-Min Liao was born in Taoyuan, Taiwan, on February 24, 1997. He is currently working toward the master's degree with the Department of Electrical Engineering, National Central University, Taoyuan, Taiwan. His current research interests include single-photon avalanche diode and avalanche photodiode.

Authorized licensed use limited to: National Central University. Downloaded on May 19,2022 at 05:53:44 UTC from IEEE Xplore. Restrictions apply.

Po-Shun Wang was born in Kaohsiung, Taiwan, on June 2, 1998. He is currently working toward the master's degree with the Department of Electrical Engineering, National Central University, Taoyuan, Taiwan. His current research interests include single-photon avalanche diode and avalanche photodiode.

Sean Yang received the B.S. degree in electrical engineering from National Taiwan Ocean University, Taiwan, in 2006 and then started working with E Ink Holdings Inc., as Photo Engineer, from 2006 to 2017. He is currently working with Source Photonics Inc., as Engineer of advanced tools.

Sheng-Yun Wang received the B.S. degree in physics from National Tsing Hua University, Taiwan, in 2006, and the M.S. degree in electrophysics from National Chiao Tung University, Taiwan, in 2008. He is currently working with Source Photonics Inc., as Sr. Engineer of Rx products.

Hsiang-Szu Chang received the M.S. and Ph.D. degrees from Solid-State Optics Lab, from the Department of physics, National Central University, Taiwan, in 2002 and 2009, respectively. He is currently working with Source photonics Inc., as a Sr. Engineer of Product Development, OE device.

H.-S. Chen received the Ph.D. degree from the Graduate Institute of Photonics and Optoelectronics, from the Nation Taiwan University, Taiwan, in 2006. Since June 2007, he has been a Postdoctoral Research Fellow with the Institute of Physics, Acadmia Sinica. From 2011 to 2013, he was with the Institute of Photonics and Optoelectronics, Nation Taiwan University, as a Postdoctoral Fellow. His research interests include surface plasmon, near field optics, ultrafast laser, nanorod array LED and optical sensors. In 2014, he joined the Source Photonics Inc., as a Manager of Advanced Process Development.

Jack Jia-Sheng Huang received the B.S. degree in physics from National Taiwan University, Taiwan, in 1992, and the M.S. and Ph.D. degrees in materials science from the University of California, Los Angeles (UCLA), United States, in 1996 and 1997, respectively. In 1997, he was the recipient of the Outstanding Ph.D. Award and Dissertation Year Fellowship Award from Henry Samueli School of Engineering, UCLA. He is currently a Sr. R&D Scientist/Manager with Source Photonics, working on Advanced Photonics Devices including 100G DML, 40G CWDM DFB, 10G DFB and 10G FP lasers as well as 10G and 25G APD photodetectors. His R&D projects also involve device reliability physics and device characterization. He has more than 90 publications in international journals and conferences in the areas of optoelectronics and ICs. He holds six US patents and one U.K. patent. From 2000 to 2015, he was a Wafer Fab R&D/Operations manager with Emcore, working on devicedesign/process/characterization, reliability, electrostatic discharge (ESD) and failure analysis of analog BH lasers and digital ridge lasers for cooled and uncooled applications. From 1997 to 2000, he was a Member of Technical Staff with Lucent Technologies, Bell Labs, Orlando, FL, working on electromigration, stress migration and failure analysis of 0.3, 0.25, 0.2 and 0.16 mm ASIC and FPGA devices using CMOS technology. During 1992–1993, he was a Research Assistant with the Institute of Atomic and Molecular Sciences, Academia Sinica, Taiwan, studying surface physics of gallium ion beam in ultra-high vacuum.

Emin Chou received the B.S. degree in nuclear engineering from National Tsing Hua University, Taiwan, in 1997, and the M.S. degree from the MBE lab, Department of Electronics Engineering, National Chiao Tung University, Taiwan, in 1999. He is currently working with Source Photonics Inc., as the Sr. Director of Product Development, Advanced OSA and OE Devices.

Yu-Heng Jan was born in Taipei, Taiwan, on November 6, 1965. He received the Ph.D. degree in electrical and computer engineering from the University of California, Santa Barbara, in 1997. In 1997, he joined the Optical Division of MRV Communication, where he focused on the design and manufacturing of CWDM DFB lasers and systems. In 2007, he became the COO and General Manager of Taiwan division of Source Photonics, where he managed Operations and RD activities. He was the Chief Device Officer with Source Photonics, where he focused on high speed devices for Data Center and PON applications.

Jin-Wei Shi (Senior Member, IEEE) was born in Kaohsiung, Taiwan, on January 22, 1976. In 2003, he joined the Department of Electrical Engineering, National Central University, Taoyuan, Taiwan, where he has been a Professor since 2011. In 2011–2012 and 2016–2017, he joined the ECE Department of UCSB as a Visiting Professor. He has authored or coauthored more than four book chapters, 150 journal papers, 200 conference papers and holds 30 patents. His current research interests include ultra-high speed/power photodetectors, electro-absorption modulators, THz photonic transmitters, and VCSELs. In 2010, he was the recipient of the Da-You Wu Memorial Award.

Authorized licensed use limited to: National Central University. Downloaded on May 19,2022 at 05:53:44 UTC from IEEE Xplore. Restrictions apply.